

# Electrical current distribution across a metal-insulator-metal structure during bistable switching

C. Rossel,\* G. I. Meijer, D. Brémaud, and D. Widmer

*IBM Research, Zurich Research Laboratory, CH-8803 Rüschlikon, Switzerland*

Combining scanning electron microscopy (SEM) and electron-beam-induced current (EBIC) imaging with transport measurements, it is shown that the current flowing across a two-terminal oxide-based capacitor-like structure is preferentially confined in areas localized at defects. As the thin-film device switches between two different resistance states, the distribution and intensity of the current paths, appearing as bright spots, change. This implies that switching and memory effects are mainly determined by the conducting properties along such paths. A model based on the storage and release of charge carriers within the insulator seems adequate to explain the observed memory effect.

61.16.Bg, 68.55.-a, 72.20.Jv, 73.40.Rw

## I. INTRODUCTION

The use of thin-film heterostructures for making two-terminal switching and memory devices has been a long-standing challenge. Much work has been done in the field, starting already in the late sixties on various materials such as amorphous semiconductors [1,2,3], ZnSe-Ge heterojunctions [4] as well as on several binary oxides [5,6,7,8,9] to produce simple crosspoint memory arrays with bit and word lines. More recently, work on porous Si [10] and polymers [11,12,13] has also demonstrated electrical bistability. The enhanced interest in perovskites since the discovery of high-temperature superconductivity in the cuprates and the giant and colossal magnetoresistance in the manganites has generated a tremendous effort in the investigation of oxide thin films. In particular the replacement of SiO<sub>2</sub> as gate oxides in CMOS technology and the fabrication of smaller ferroelectric memories (FRAM) have triggered the research of new, alternative materials. Earlier, we reported the observation of reproducible switching and memory in Cr-doped (Ba,Sr)TiO<sub>3</sub> and SrZrO<sub>3</sub> epitaxial-film-based metal-insulator-metal (MIM) devices [14]. In particular it was shown that not only was reversible switching between a low-resistance and a high-resistance state possible but also that multilevel switching could be achieved. In addition, a retention-time test performed over 12 months demonstrated the nonvolatile memory properties of these memory cells. Nevertheless an important issue is the scalability of such devices to lower dimensions and the influence of intrinsic film defects on the current flow and the switching mechanism itself. Here we report on the simultaneous investigation of the film microstructure by scanning electron microscopy (SEM), the distribution of the electrical current flow by electron-beam-induced current (EBIC), and the switching properties of individual memory cells.

## II. EXPERIMENTAL

### A. Oxide thin films and heterostructures

The MIM structure is shown in the inset of Fig. 1. As a base metallic electrode a SrRuO<sub>3</sub> film of about 4 nm is grown epitaxially on SrTiO<sub>3</sub> (001) by pulsed laser deposition (PLD) at 700°C and an O<sub>2</sub> pressure of 250 mTorr using a KrF excimer laser. The insulating oxide film is then deposited in situ at a slightly higher temperature in a typical thickness of approx. 35 nm as determined by X-ray diffraction from the finite-size oscillations observed at low angles and at the main Bragg reflections. We focus here on SrZrO<sub>3</sub> films doped with 0.2 at.% Cr (i.e.,  $3 \times 10^{19}$  at/cm<sup>3</sup>), which were found earlier to yield good switching properties [14]. The top electrodes of Pt are evaporated by electron beam through a shadow mask to define squares or disks of variable sizes, ranging between 460 and 35  $\mu$ m, which corresponds to areas between about  $2 \times 10^{-3}$  and  $10^{-5}$  cm<sup>2</sup>. The epitaxy of the films was checked by X-ray diffraction, the surface topography by atomic force microscopy (AFM) imaging. Transport measurements were performed either in ac mode with a LCR meter HP4263 or in dc mode using a Keithley 238 current source measuring unit run in voltage- or current-controlled mode. Voltage is applied to the top electrode via a CuBe-coated tungsten needle. A current limitation is set to prevent breakdown and destruction of the structures. A typical dependence of the resistance and capacitance as a function of pad area  $A$  is shown in Fig. 1 for a 35-nm-thick SrZrO<sub>3</sub>(0.2% Cr) film. In this range of pad sizes, the resistance largely follows the  $R \propto A^{-1}$  relation as shown on a log-log plot, whereas the capacitance increases linearly with  $A$ , leading to a dielectric constant of about 28.

From these scaling properties, it appears that the film transport properties are rather homogeneous down to a

---

\*To whom correspondence should be addressed; e-mail: rsl@zurich.ibm.com

length scale of about 50  $\mu\text{m}$ . Below, they become more strongly dependent on the distribution of microstructural defects such as grain boundaries, precipitates of other phases or micro pinholes, and a systematic scaling analysis is more difficult. Pad sizes down to 100 nm were successfully patterned on thinner films by electron-beam lithography and lift-off techniques [15] and investigated by AFM with a conducting tip [16]. Switching by voltage pulses was observed, but a systematic analysis was difficult because of local inhomogeneities and varying sticking properties of the metal pads.

### B. Electron-beam-induced current method

EBIC has primarily been used to investigate the electrical properties of metal-oxide-semiconductor (MOS) capacitors, focussing on the leakage and breakdown properties of oxide thin films grown on Si [17,18,19,20,21]. In those cases an internal electrical field allows the specimen to act as detector of the charge carriers generated by the incident electron beam. The injected carriers are subject to drift, diffusion, trapping and recombination events. The formation of a space charge region at the interface with the bulk Si (*p*-type or *n*-type) separates the electron-hole pairs created by each absorbed electron, resulting in a large current gain [18]. The output signal can be amplified by several orders of magnitude. Performing EBIC in a SEM provides a way to map and quantify the inhomogeneities in the electrical properties of a material that are due to several types of intrinsic defects. Since the pioneering work of Pensak [22], to our knowledge, very few EBIC studies have been done on MIM structures, such as ours, using an insulating oxide epitaxially grown on a metallic oxide base electrode. The diagram of the experimental arrangement is shown in Fig. 2. A JEOL 6400 scanning microscope has been equipped with a custom-made removable micromanipulator. The electrical contact to the top electrode is done with a CuBe-coated tungsten needle. Bias polarity is defined with reference to the  $\text{SrRuO}_3$  bottom electrode connected with silver paint to a thin Cu wire. The low-noise EBIC amplifier (Keithley 428) is connected to the sample in the vacuum chamber by coaxial feedthroughs. A useful aspect of the circuit is the current suppression option, which enables subtraction of the background signal. The data-acquisition system consists of a digital imaging scanning unit (WinDiss-2 from Point Electronic GmbH, Halle, Germany) with two analog 12-bit input channels. For the measurements, the electron-beam energies  $E_b$  were varied between 20 and 30 kV with beam currents  $I_b$  ranging from 0.1 to 7 nA, as verified by a Faraday cup.

## III. RESULTS

The first EBIC measurements coupled to electrical switching were done using rather thick, 100-nm Pt top

electrodes to ensure that the tip did not scratch or perforate the  $\text{SrZrO}_3$  oxide layer (same film as for Fig. 1). In all memory cells investigated, the EBIC images taken in the high-resistive state systematically showed a given number of white spots corresponding to discrete paths of flowing current (Fig. 3). Most of the pictures are taken at small ( $< 1$  V) or zero voltage because the application of larger bias up to  $\pm 5$  V lead to enhanced background noise without changing the image features. As expected, a change of the bias polarity produced an inversion of the image contrast. Even when displacing the needle slightly, no change in the flow configuration was observed and no visible current path was generated by the pressure of the needle at the contact location. Thus the main current flow seems to be restricted around some of the defects in the  $\text{SrZrO}_3$  film, but not all defects contribute to it. This point is supported by Fig. 3(c,d), which is an enlarged view of the Pt electrode surface. Next to a small circular hole in the Pt, 350 nm in diameter, a protuberance of similar size pops up because of an underlying defect in the oxide film [Fig. 3(c)]. The corresponding EBIC image [Fig. 3(d)] shows that the current flows only on that defect and not through the hole. Other smaller defects and visible surface particles, possibly dust, do not generate any electron-beam-induced currents at this sensitivity scale. Because of diffused electrons in the various layers, the radius of the white spot is not a uniquely defined quantity here as it depends on the amplification gain and on intensity and contrast factors of the scanned image. At low current densities, a lateral resolution of 20 nm can be achieved with our system.

An interesting observation was made when focusing the entire electron beam on one of the conducting spots. By applying the maximum beam current ( $I_b = 18$  nA) at 35 kV for successive periods of time (1 to 30 min), a series of SEM/EBIC images were taken under the same conditions ( $E_b = 25$  kV;  $I_b = 1.5$  nA). Surprisingly, the intensity (and radius) of the spot decreased progressively until it became almost invisible, whereas the corresponding resistance of the MIM structure measured at 0.2 V increased by about 8% from 730 to approx. 790 k $\Omega$ . The direct influence of a carbon film grown by the incident beam should be negligible as long as the underlying Pt layer is not removed or modified. We found in addition that not all the spots treated in that manner could be made to fully disappear. A possible reason for this extinction effect will be discussed below.

### A. Bistable switching and EBIC

Let us now turn to the correspondence between electrical switching and the EBIC images. For this purpose we have grown similar films with thinner (4–5 nm) top Pt electrodes. Under these conditions, the microstructure and defects of the films under the metal electrode can be seen with surprisingly good contrast and accuracy. A sequence of four EBIC pictures is displayed in Fig. 4

with the corresponding  $I$ - $V$  characteristics defining the resistance state of a memory cell  $175\text{ }\mu\text{m}$  in diameter. In the initial high-resistance state, typically  $750\text{ k}\Omega$ , one observes about 10 white spots of various sizes distributed across the electrode in the EBIC picture [Fig. 4(a)]. In this stage, a set of symmetric and reversible  $I$ - $V$  characteristics was taken at a rate of  $0.1$  to  $0.2\text{ V/s}$ , starting from the maximum positive bias voltage,  $V_{\text{max}}$ . By progressively increasing  $V_{\text{max}}$ , the cell started to switch partially for a maximum bias of  $7\text{ V}$  and a compliance current of  $200\text{ }\mu\text{A}$ , as seen from the dashed curve 1 in Fig. 4(a). From the respective slopes at zero bias, a resistance ratio  $r = R_{\text{high}}/R_{\text{low}} = 22$  was derived. In the following run, the sample, which was not completely preformed, returned to its high-resistance state (reversible curve 2). When increasing the voltage to  $8\text{ V}$  and the limiting compliance to  $350\text{ }\mu\text{A}$ , bistable and reproducible switching set in. The next run was then stopped at  $0\text{ V}$  after sweeping to negative voltage and switching the memory cell into its low-resistance state ( $R_{\text{low}} = 11.6\text{ k}\Omega$ ) [Fig. 4(b)]. In that state a new EBIC image was scanned showing the clear appearance of two new intense spots (see arrows). The intensity of the other spots remained practically unchanged. As the device was switched back to its high-resistance state ( $606\text{ k}\Omega$ ) after a sweep up to  $8\text{ V}$  and down to  $0\text{ V}$ , the two spots disappeared almost completely [Fig. 4(c)]. At the same time some of the existing spots became slightly more intense. To check whether the current-path distribution was reversible, the cell was switched back to its low-resistance state ( $R_{\text{low}} = 10.5\text{ k}\Omega$ ) through an entire cycle so as to start the sweep again from positive bias voltage. Surprisingly, only one of the two previous spots reappeared, accompanied by three new intense spots [arrows, Fig. 4(d)]. This observation leads us to conclude that electrical switching in thin films correlates to a large extent to the properties of individual conducting paths that can be locally turned on and off or changed in intensity. These paths are located at the positions of intrinsic defects in the film. Nevertheless at low current amplitudes or in a very high resistive state, an homogeneous contribution of the bulk of the film cannot be ruled out. In the present case, if one assumes that the entire current of  $400\text{ }\mu\text{A}$  flows along about 15 channels having an average area of  $10\text{ }\mu\text{m}^2$ , we get a rather high current density of  $4 \times 10^3\text{ A/cm}^2$ .

After this treatment the cell was switched back and forth many times, keeping it either in the low- or the high-resistance state at zero bias voltage for up to  $48\text{ h}$  without any change, confirming the nonvolatility of the given state. In the dc mode, the switching ratio  $r = R_{\text{high}}/R_{\text{low}}$  was found to vary between approx. 45 and 90, depending on the amplitude of the compliance current set to prevent breakdown. Fast switching was also performed by application of short pulses for writing and erasing, as described in [14]. In this mode we observed that for a given voltage pulse amplitude, the ratio  $r$  increases continuously with the pulse length between  $1\text{ ms}$  and  $1\text{ s}$ , i.e., the total number of charges injected into the insulator plays the

dominant role in the switching mechanism. After several experiments at increasingly higher current values, the memory cell became locked into its low-resistance state. Nevertheless, by applying a constant voltage of  $9\text{ V}$  for a longer time, the cell can be repaired and partially restored into its high resistive state. As shown in Fig. 5, the current measured over a period of  $14\text{ h}$  decreased continuously, with a change in resistance from  $25$  to  $118\text{ k}\Omega$  measured at  $0.2\text{ V}$ . This time dependence can be well fitted by a double exponential decay function of the form  $I(t) = I_0 + A_1 \exp(-t/\tau_1) + A_2 \exp(-t/\tau_2)$ , with long time constants  $\tau_1 = 0.52\text{ h}$  and  $\tau_2 = 11.8\text{ h}$ . At that stage the device was stable and could again be switched with pulses. This means that the conducting paths have been modified by this forming process.

## B. Microstructural defects

The important question that arises at this point is the nature of the defects and their individual electronic properties. If bistable switching is by nature related to the conduction processes of one or several local paths, it would be favorable to control their number or artificially recreate their structure. Such work is under way on specially dimpled single crystals of Cr-doped  $\text{SrTiO}_3$ .

EBIC images can strongly enhance microstructural details that are not visible in conventional SEM images of collected secondary electrons. This contrast enhancement is true for MOS devices [18], but especially so in MIM structures. As an example two enlarged sections of the surface of the memory cell measured above are displayed in Fig. 6. The EBIC image of Fig. 6(a) shows the Pt electrode ( $5\text{-nm}$  thick), its rounded edge with decreasing thickness (shadow effect) and the  $\text{SrZrO}_3$  film underneath. Next to the two white conducting spots, a number of black dots, smaller than  $500\text{ nm}$  in diameter and surrounded by a dark halo ( $2\text{--}5\text{ }\mu\text{m}$ ), are scattered across the Pt surface. These features are only seen for a thin Pt layer and correspond to microstructural defects in the oxide film; some of them, but not all, are observable in the SEM image. Two zoomed-in views corresponding to the white rectangle and taken under a tilt angle of  $37^\circ$  are displayed in Fig. 6(b) and (c). The SEM picture shows a smooth surface with the presence of a main dot ( $250\text{ nm}$  in diameter) at the center and a few smaller ones scattered around it. In the corresponding EBIC image, the main defect is clearly visible with its surrounding cloud, but, more interestingly, the granularity of the nanostructure of the film below the platinum electrode becomes apparent with features having a typical size of  $200\text{ nm}$  or less, which corresponds to the topography found by AFM (Fig. 7). Indeed, next to the fine nanostructure displayed in the AFM image, bright and darker regions defining hillocks and dips of about  $200\text{ nm}$  are in evidence over the scanned area ( $1 \times 1\text{ }\mu\text{m}^2$ ). The origin of the defects seen in Fig. 6 can be partly attributed to the LPD technique itself [23]. Besides the many advan-

tages of laser ablation, some of its inherent drawbacks are the projection of microscopic ejecta during the ablation process, which can stick to the substrate, the presence of microditches or holes caused by bombardment with high-kinetic-energy particles, and the insertion of impurities present in the target material. In all these cases it cannot be excluded that their presence in the film locally creates a microstructural stress field that only becomes apparent with methods based on electron- or light-beam injection. Another explanation for the clouds in the EBIC scans could be a local modification of the interface properties between the metal electrode and the film, such as a local change in the respective work functions due to oxidation of the metal electrode and depletion of the oxide layer.

In thicker films of the same manufacture, the number of observable white spots, such as those seen in Figs. 3 or 4, is less important at small bias voltage but definitely increases at higher voltages. Once the compliance is released and the current progressively raised until thermal breakdown occurs, localized “burned” pits with crater-like geometry are generated and the structure is shorted. The interesting observation is that their number is larger than the EBIC spots observed in the pre-breakdown regime but all EBIC spots correspond to a “burned” channel. The general coincidence of breakdown sites with defects such as stacking faults and the contrast mechanisms at these sites have been studied by many researchers but almost exclusively in gate oxides grown on Si [17,18,19,20,21].

#### IV. DISCUSSION

A well-known observation in dielectric ceramics is the resistance degradation induced by dc electrical field stress [24,25]. Such a degradation, characterized by a slow increase of the leakage currents, may occur at temperatures and fields much below the onset values of dielectric or thermal breakdown. This wear-out process, which is the main limiting factor for the lifetime of multilayer ceramic capacitors, is not destructive and reversible upon annealing. From the large number of studies on oxides and in particular on perovskite ceramics such as  $\text{SrTiO}_3$  [24,26,27,28], it appears that the degradation rate is largely influenced by grain size, stoichiometry, doping, second phases, porosity, and electrode properties. In general, doping with donors such as  $\text{La}^{3+}$ , which goes into the A sites (e.g.,  $\text{Sr}^{2+}$ ) of the  $\text{ABO}_3$  perovskite lattice, leads to an increase of the leakage current and improves or stabilizes the degradation [29]. On the other hand, acceptor dopants such as  $\text{Al}^{3+}$ ,  $\text{Fe}^{3+}$ ,  $\text{Mn}^{3+}$ , or  $\text{Cr}^{3+}$  [29,30], which partially substitute on the B site (e.g.  $\text{Ti}^{4+}$ ), lead to a significant decrease in the leakage and relaxation currents and to a suppression of the degradation rate. As mentioned by Waser *et al.* [26,27] the current response of high- $K$  thin films under a voltage step excitation exhibits three distinct regimes: a short-term relaxation regime with a power-law decay  $J \propto t^{-\alpha}$

( $\alpha \simeq 1$ ) attributed to bulk microstructural effects (i.e., degree of crystallinity), a mid-term leakage regime with little change in  $J$  (electrode interface and bulk-doping effects), followed by a resistance degradation regime with increasing  $J$ . This last regime, which is well understood in titanate single crystals [31], is more complicated in thin films and seems to be induced both by electronic and ionic transport. Clearly, the double exponential decay law that we observe in the recovery phase of our film in Fig. 5 under rather high electrical fields ( $E = 2.6 \times 10^8$  V/m) is different from the above-mentioned power law valid for a pristine film at lower field. This behavior would point towards a different mechanism dominated by the flow of the current in localized channels rather than homogeneously across the bulk of the film.

If this idea is correct, as our EBIC experiment indicates, it is to be expected that the mechanism for switching and memory is also dominated by the properties of such channels or filaments. One reason is that switching never occurs without forming the material, i.e., reducing its resistance from the  $\text{M}\Omega$ – $\text{G}\Omega$  range to the  $\text{k}\Omega$ – $\text{M}\Omega$  range. During forming, the weaker regions of the dielectric undergo an enhanced electric-field stress and become more suitable for the flow of current. This current is mainly due to the hopping or tunneling of charges between adjacent sites or traps localized in the gap of the insulator. A possible mechanism can be related to the filling and defilling of traps by impact or field ionization as proposed by several authors [4]. One very appealing model is that of Simmons and Verderber [32] proposed earlier to explain voltage-controlled negative resistance and reversible memory effects in thin films of  $\text{SiO}$  sandwiched between Al and Au electrodes. The idea is that a broad band of localized states is created in the insulating gap by doping and forming. In our case we can expect that the doping with  $\text{Cr}^{3+/4+}$  ions ( $3 \times 10^{19}/\text{cm}^3$ ) creates such sites separated by about 3 nm, in addition to the intrinsic traps. This separation is short enough to favor a tunneling process for the transport of electrons injected from the cathode. Assuming that the occupation probability of these sites is determined by the kinetics of tunneling rather than thermal statistics (small Boltzmann term) and that the energy of the electron is conserved during tunnel transition, Simmons and Verderber [32] suggested an  $I$ – $V$  curve of the form  $I = a \sinh(bV)$  for the low-impedance state. The coefficient  $a = A \exp(-1.02s(\phi_0 - \frac{1}{2}E_0s)^{1/2})$  is a transition probability, where  $A$  is a constant,  $\phi_0$  the metal-insulator barrier height,  $s$  the average inter-site spacing, and  $E_0 = -Q_0/K\epsilon_0$  the electrical field at the cathode-film interface derived from Poisson’s equation.  $Q_0$  is the total uncompensated charge in the depletion region of the insulator. The second factor is  $b = 0.13s^2/(\phi_0 - \frac{1}{2}E_0s)^{1/2}$ . To explain the memory effect, characterized by the presence of an hysteresis loop in the  $I$ – $V$  cycle, it is assumed that charges can be stored in the insulator when the applied voltage exceeds a certain threshold equivalent to the energy  $\phi_i$  defining the

top of the localized levels with respect to the Fermi level. The storage of negative charges  $qN_s$  near the top of the localized band in the insulator reduces the electrical field at the interface to  $E'_0 = -(Q_0 - qN_s/2)/K\epsilon_0$ , and consequently the current passing through the system is lower, according to the above equation for  $I(V)$ , in which  $E_0$  is replaced by  $E'_0$ . Thus a higher impedance state is reached by storing trapped charges, whereas the lower impedance state is reestablished by releasing them. The ratio of the two impedances at  $V = 0$  is therefore given by the amount of charge that can be stored in the system. This also explains why multilevel switching can be achieved in our thin films by the application of voltage pulses of different heights [14]. The relevant quantity is in fact the amplitude of the current pulse times its width, which determines the total amount of charge storage. According to our observations, it appears that if the pulses are too short for a given amplitude or if the interval between two successive pulses is too small, the memory effect tends to vanish. A plausible explanation for the observed dead time is that the stored charges need a finite time to migrate to the center of the insulator, possibly by a phonon-assisted tunneling process, before they can escape.

To check the validity of this model at room temperature, we have fitted the  $I$ - $V$  curves corresponding to the high- and low-impedance states of Fig. 4 with the above equation  $I = a \sinh(bV)$ . It is found that the  $I$ - $V$  curves of both states can be very well adjusted to the  $\sinh(V)$  dependences, in support of the model. We have also compared our fits with other expressions describing carrier transport in insulators, such as those for Schottky, Frenkel-Poole and Fowler-Nordheim field emissions, as well as space-charge-limited conduction [25,33]. It appears that the high-impedance  $I$ - $V$  curves can also be fitted with the equation  $I = \alpha V \exp(\beta\sqrt{V}/T - q\phi_0/kT)$  known for Frenkel-Poole emission, where the conduction is due to field-enhanced thermal excitation of trapped electrons into the conduction band. Here  $\alpha$  and  $\beta$  are two constants. Nevertheless additional attempts with the expression derived for the tunnel or field emission in the Fowler-Nordheim regime, i.e.,  $I = \alpha V^2 \exp(-\beta/V)$ , failed. In that case the tunnel emission is caused by field ionization of trapped electrons into the conduction band or by tunneling from the metal Fermi level into the insulator conduction band. This mechanism is expected to apply only at higher voltages, above the threshold at which the memory cell switches. Concerning the low-impedance state, satisfactory fits could only be achieved with the Frenkel-Poole model or with an expression of the type  $I = \alpha V + \beta V^2$ . Here the ohmic dependence at low field is the result of thermally excited charges hopping between adjacent isolated states, whereas the quadratic term corresponds to a space-charge-limited current resulting from the injection of carriers into an insulator with no compensating charges. Based on the analysis of the  $I$ - $V$  curves in both impedance states, it seems that several transport mechanisms based on hopping or tunneling through the insulator are possible, but the model

of Simmons and Verderber is very appealing because it agrees with our data and provides a good explanation of the nonvolatile memory effect in terms of the storage and release of charges. It even provides an explanation of multilevel switching and the various requirements for the pulse amplitudes, widths and sequences. Further investigations in particular on the temperature dependence of the switching and memory effect, are needed to confirm or refine the model. Indeed, we know that the switching effect is temperature dependent and tends to vanish around 400 K. Current measured in both high- and low-impedance states down to 77 K exhibits a thermally activated behavior [14]. In view of our EBIC results on films, where the filamentary distribution of the electrical current has been visualized and demonstrated, it nevertheless seems more appropriate to investigate a system with a single, well-controlled channel, possibly in a defect- and stress-free single crystals or in a fully amorphous oxide layer. Finally, the extinction of the EBIC spots under intense electron-beam injection and its correlation to a resistance increase as mentioned above can be understood by the proposed model. The strong electron injection in a given channel fills all available traps in the localized band and reduces the intersite tunneling probability to zero.

## V. CONCLUSIONS

The EBIC technique evidently is of great use for investigating MIM capacitors with switching and memory properties. First it is observed that current-leakage sites (white spots) coincide with local defects in the film. The size of these defects (nanoditches, impurities, grain boundaries) which is inherent to film growth, can be very small, typically less than a few hundred nanometers. Thanks to the enhanced contrast of the EBIC method it is possible to observe details of the microstructures of the film below the thin (5-nm) electrode that are not observable by simple secondary electron SEM imaging. The second observation is that the switching of the impedance state of the memory cell is correlated to the number and intensity of the current-leakage paths. This is demonstrated by a correlated measurement of the  $I$ - $V$  characteristics of the device and its EBIC imaging. The self-similarity of the film's microstructure can explain why switching and memory effects can in principle be observed in such heterostructures down to very small length scales. According to our previous observations, doping with a rather high concentration of Cr ions ( $10^{19}/\text{cm}^3$ ) seems to help in stabilizing the switching effect in the perovskites investigated [14]. These ions act as local traps within the insulator, and in addition to other intrinsic defects form a broad band of localized states. Switching and nonvolatile memory can well be explained by a model based on tunneling conduction between adjacent sites and on the storage or release of charges in traps at the top of the localized band [32]. The  $I$ - $V$

dependence proposed in this model is in agreement with our measurements. There is no reason to doubt that such a mechanism imagined for the bulk of a material is also valid in the core of a leakage path in the prebreakdown regime. Therefore it would be relevant to create such leakage paths with stable and reproducible switching and memory properties in a controlled manner if one wishes to manufacture large arrays of crosspoint memories based on two-terminal devices.

## ACKNOWLEDGMENTS

The authors wish to thank Ch. Gerber for investigating the films by AFM imaging, M. Tschudy for evaporating the metal electrodes, and M. Despont for introducing us to the manipulation of the JEOL SEM microscope. Fruitful discussions with J. G. Bednorz, R. Allenspach and M. Roulin as well as the continuous support of P. F. Seidler during this work are gratefully acknowledged.

- 
- [1] S. R. Ovshinsky, Phys. Rev. Lett. **36**, 1469 (1968).  
[2] R. G. Neale and J. A. Aseltine, IEEE Trans. Electron Dev. **20**, 195 (1973).  
[3] J. F. Dewald, A. D. Pearson, W. R. Northover, and W. F. Peck, Jr., J. Electrochem. Soc. **109**, 243c (1962).  
[4] H. J. Hovel and J. J. Urgell, J. Appl. Phys. **42**, 5076 (1971).  
[5] W. R. Hiatt and T. W. Hickmott, Appl. Phys. Lett. **6**, 106 (1965).  
[6] T. W. Hickmott, J. Vac. Sci. Technol. **6**, 828 (1969).  
[7] K. L. Chopra, J. Appl. Phys. **36**, 184 (1965).  
[8] F. Argall, Solid State Electron. **11**, 535 (1968).  
[9] J. F. Gibbons and W. E. Beadle, Solid State Electron. **7**, 785 (1964).  
[10] K. Ueno and N. Koshida, Appl. Phys. Lett. **74**, 93 (1999).  
[11] H. J. Gao, K. Sohlberg, Z. Q. Xue, H.Y. Chen, S. M. Hou, L. P. Ma, X. W. Fang, S.J. Pang, and S. J. Pennycook, Phys. Rev. Lett. **84**, 1780 (2000).  
[12] S. G. Liu, P. J. Wu, Y. Q. Liu, and D. B. Zhu, Mol. Cryst. Liq. Cryst. **275**, 211 (1996).  
[13] J. H. Krieger, N. F. Yndanov, I. K. Igumenov, and S. V. Vaschenko, J. Structural Chem. **34**, 966 (1993).  
[14] A. Beck, J. G. Bednorz, Ch. Gerber, C. Rossel, and D. Widmer, Appl. Phys. Lett. **77**, 139 (2000).  
[15] Work performed by Shalom Wind at IBM Research, T. J. Watson Research Center, Yorktown Heights, NY.  
[16] A. Bietsch, unpublished results.  
[17] P. S. D. Lin and H. J. Leamy, Appl. Phys. Lett. **42**, 717 (1983).  
[18] H. R. Kirk, Z. Radzimski, A. Buczkowski, and G. A. Rozgonyi, IEEE Trans. Electron Dev. **41**, 959 (1994); *idem*, J. Electrochem. Soc. **146**, 1529 (1999).  
[19] M. Tamatsuka and K. Miki, Solid State Phenomena **63-64**, 295 (1998).  
[20] W. S. Lau, D. S. H. Chan, J. C. H. Phang, K. W. Chow, K. S. Pey, Y. P. Lim, and B. Cronquist, Appl. Phys. Lett. **63**, 2240 (1993).  
[21] P. S. D. Lin, R. B. Marcus, and T. T. Sheng, J. Electrochem. Soc., Solid State Science and Technology **130**, 1878 (1983).  
[22] L. Pensak, Phys. Rev. **75**, 472 (1949).  
[23] P. R. Willmott and J. R. Huber, Rev. Mod. Phys. **72**, 319 (2000).  
[24] *Werkstoffe und Bauelemente der Elektrotechnik, Keramik*, edited by H. Schaumburg (B. G. Teubner, Stuttgart, 1994).  
[25] J. J. O'Dwyer, *The Theory of Electrical Conduction and Breakdown in Solid Dielectrics* (Clarendon Press, Oxford, 1973).  
[26] R. Waser, T. Baiatu and K. H. Härdtl, J. Am. Ceram. Soc. **73**, 1645 and 1654 (1990).  
[27] R. Waser, J. Am. Ceram. Soc. **72**, 2234 (1989).  
[28] G. W. Dietz, M. Schumacher, R. Waser, S. K. Streiffer, C. Basceri, A. I. Kingon, J. Appl. Phys. **82**, 2359 (1997).  
[29] W. Hofman, S. Hoffman, and R. Waser, Thin Solid Films **305**, 66 (1997).  
[30] S. H. Paek, E. S. Lee, S. H. Kim, J. Y. Seong, J. P. Mah, C. S. Park, J. S. Choi, and J. H. Jung, J. Mater. Sci. **33**, 1239 (1998).  
[31] T. Baiatu, R. Waser, and K. H. Härdtl, J. Am. Ceram. Soc. **73**, 1663 (1990).  
[32] J. G. Simmons and R. R. Verderber, Proc. Roy. Soc. A **301**, 77 (1967).  
[33] S. M. Sze, *Physics of Semiconductor Devices*, 2nd edition (John Wiley & Sons Inc., New York, 1981).

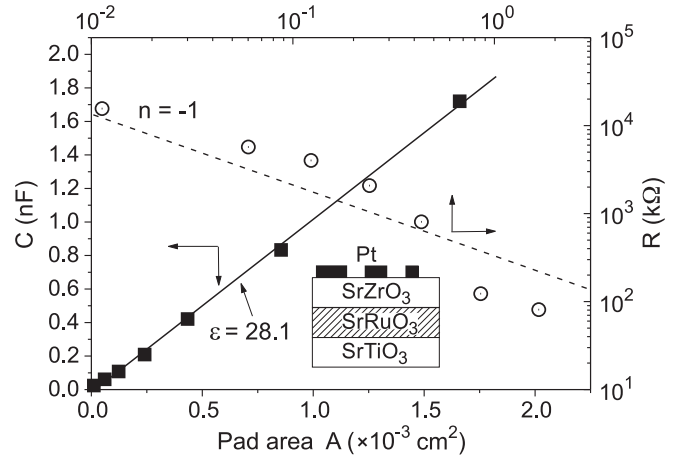


FIG. 1. Capacitance and resistance (log-log plot) versus pad area of a Pt/SrZrO<sub>3</sub>(0.2% Cr)/SrRuO<sub>3</sub>/SrTiO<sub>3</sub>(001) MIM structure at 300 K. The SrZrO<sub>3</sub> film is 35 nm thick. Both dependences point to a good scaling down to the smallest pad size, 40  $\mu\text{m}$  in diameter.

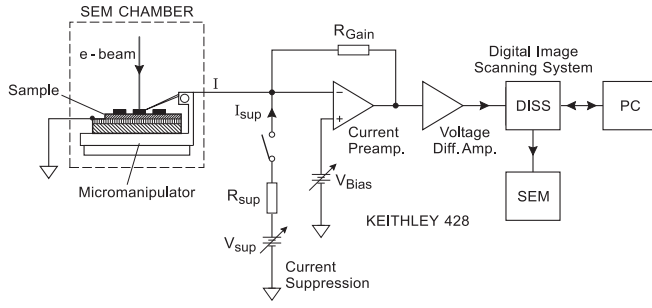


FIG. 2. Schematics of the EBIC measurement system.

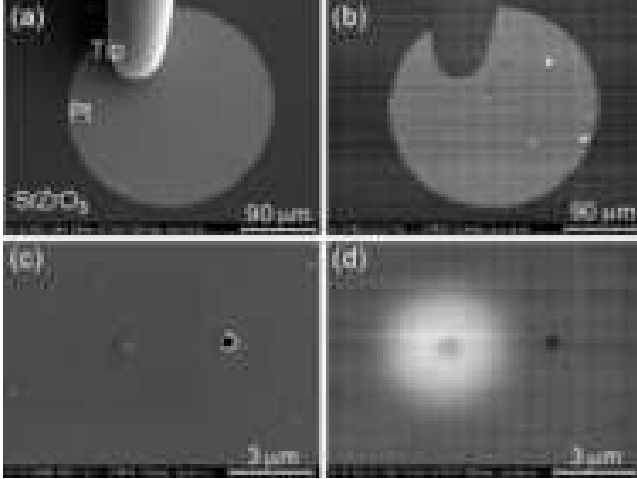


FIG. 3. (a) SEM image of a Pt/SrZrO<sub>3</sub>(0.2% Cr)/SrRuO<sub>3</sub> MIM capacitor structure with Pt electrode, 250  $\mu\text{m}$  in diameter and 100 nm thick. (b) Corresponding EBIC image at  $V_b = 0$  V with the appearance of conducting white spots. Beam-acceleration voltage  $V_{\text{acc}} = 25$  kV. (c) Enlarged SEM view showing a defect in the film below the Pt electrode and a hole in this electrode, and (d) corresponding EBIC image with one bright leakage spot correlated to the defect but not to the hole.

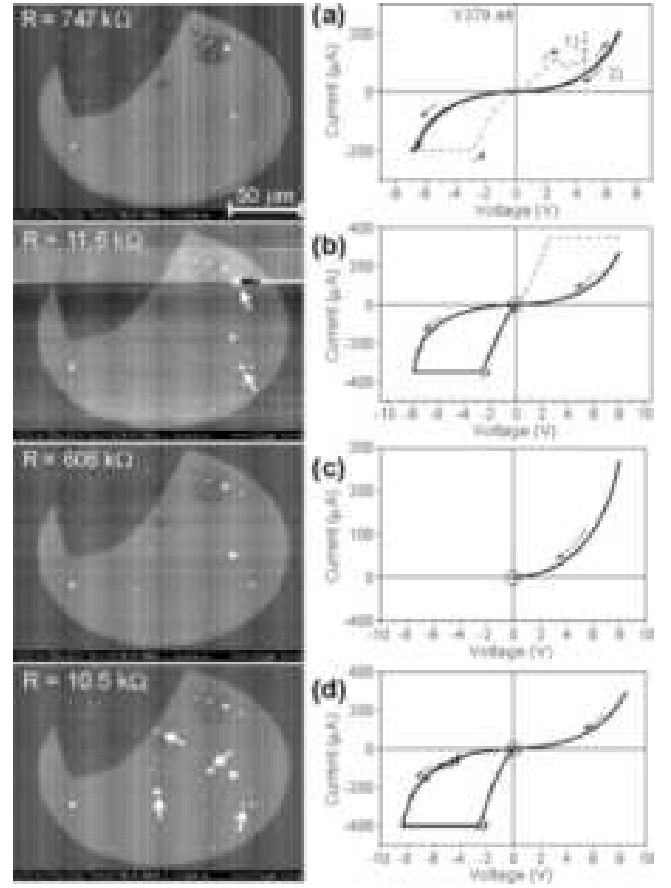


FIG. 4. Sequence of EBIC images and the corresponding  $I$ - $V$  characteristics for a Pt/SrZrO<sub>3</sub>(0.2% Cr)/SrRuO<sub>3</sub> memory cell, 175  $\mu\text{m}$  in diameter. Pt electrode thickness is 5 nm.  $V_b = 0$  V,  $V_{\text{acc}} = 25$  kV. (a) Initial high-impedance state.  $I$ - $V$  curve 1: partial switching has occurred, curve 2 the sample has not yet switched. (b) After one cycle down to  $-8$  V and up to  $0$  V, the cell has switched to its low-impedance state, and two new spots appear in the EBIC image (arrows). (c) The cycle is completed up to  $8$  V, the cell switches back to its high-impedance state at  $0$  V, and the two spots disappear. (d) Return to the high-impedance state after full cycle sweep. New spots appear (arrows).

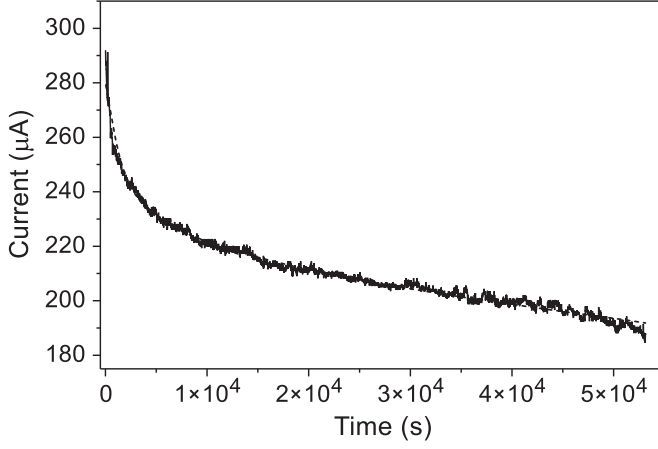


FIG. 5. Current relaxation  $I(t)$  as the memory cell is progressively returned to its higher impedance state under a stress voltage of 9 V. The data are well fitted with a double exponential decay law (dotted line).

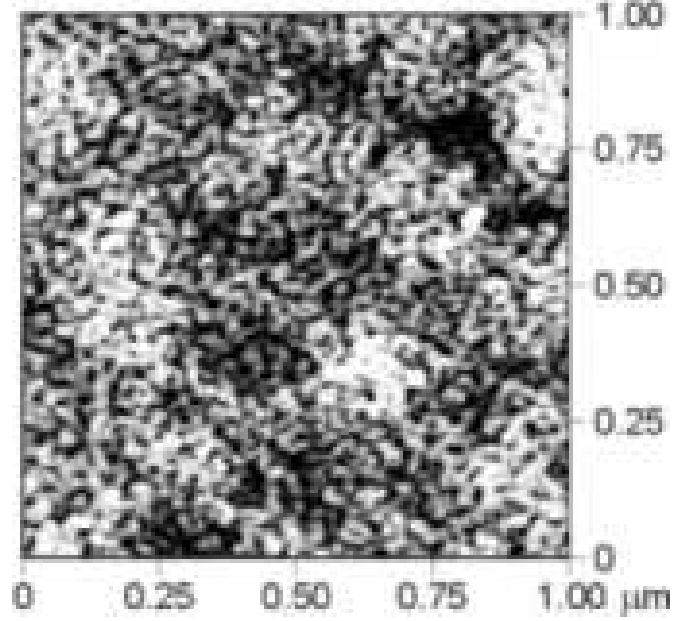


FIG. 7. AFM image of the  $\text{SrZrO}_3(0.2\% \text{ Cr})$  film grown on  $\text{SrRuO}_3/\text{SrTiO}_3(001)$  investigated in Figs. 4 to 6. Greyscale amplitude = 6.2 nm.

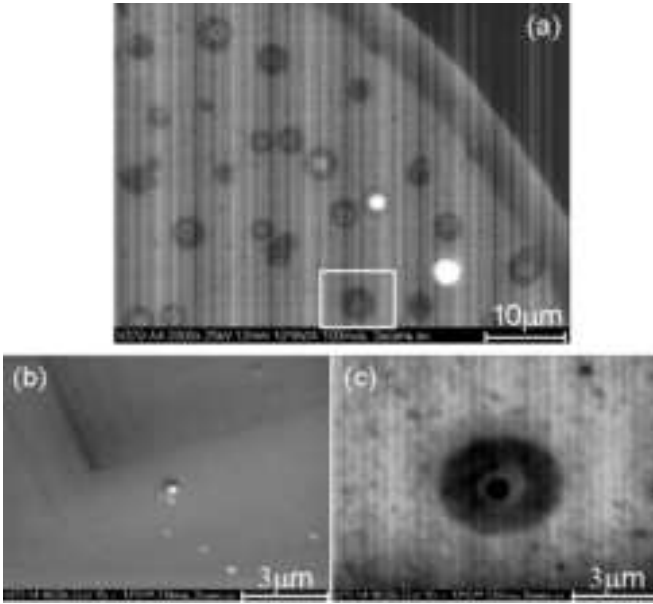


FIG. 6. (a) Enlarged EBIC image of the switching device investigated in Fig. 4, displaying two bright leakage spots and other dark spots of similar geometry corresponding to defects localized in the  $\text{SrZrO}_3$  film;  $V_b = 0 \text{ V}$ ,  $V_{\text{acc}} = 25 \text{ kV}$ . (b) SEM and (c) close-up EBIC images of the rectangular area taken under a tilt angle of  $37^\circ$ , showing the main defect and its transmitted current mapping. Sharp contrasted microstructural details of the film under the Pt layer become apparent.